Title

Crystal Chemistry and Electrochemistry of Li x Mn1.5Ni0.5O4 Solid Solution Cathode Materials

Journal

Chemistry of Materials, 29(16)

ISSN

0897-4756

Authors

Kan, Wang Hay

Kuppan, Saravanan

Cheng, Lei

et al.

Publication Date

2017-08-22

DOI

10.1021/acs.chemmater.7b01898

Peer reviewed

CHEMISTRY OF MATERIALS

Article

pubs.acs.org/cm

Crystal Chemistry and Electrochemistry of $Li_xMn_{1.5}Ni_{0.5}O_4$ Solid Solution Cathode Materials

Wang Hay Kan,[†,∥] Saravanan Kuppan,[†,∥] Lei Cheng,[†,‡] Marca Doeff,[†] Jagjit Nanda,[§] Ashfia Huq,[§,⊥] and Guoying Chen*[,†]

[†]Energy Storage and Distributed Resources Division, Lawrence Berkeley National Laboratory, Berkeley, California 94720, United States

[‡]Department of Material Sciences and Engineering, University of California, Berkeley, California 94720, United States

[§]Materials Science and Technology Division, Oak Ridge National Laboratory, Oak Ridge, Tennessee 37831, United States

[⊥]Chemical and Engineering Materials Division, Oak Ridge National Laboratory, Oak Ridge, Tennessee 37831, United States

Supporting Information

ABSTRACT: For ordered high-voltage spinel $LiMn_{1.5}Ni_{0.5}O_4$ (LMNO) with the $P4_32_1$ symmetry, the two consecutive two-phase transformations at ~4.7 V (*vs* Li^+/Li), involving three cubic phases of LMNO, $Li_{0.5}Mn_{1.5}Ni_{0.5}O_4$ ($L_{0.5}$MNO), and $Mn_{1.5}Ni_{0.5}O_4$ (MNO), have been well-established. Such a mechanism is traditionally associated with poor kinetics due to the slow movement of the phase boundaries and the large mechanical strain resulting from the volume changes among the phases, yet ordered LMNO has been shown to have excellent rate capability. In this study, we show the ability of the phases to dissolve into each other and determine their solubility limit. We characterized the properties of the formed solid solutions and investigated the role of non-equilibrium single-phase redox processes during the charge and discharge of LMNO. By using an array of advanced analytical techniques, such as soft and hard X-ray spectroscopy, transmission X-ray microscopy, and neutron/X-ray diffraction, as well as bond valence sum analysis, the present study examines the metastable nature of solid-solution phases and provides new insights in enabling cathode materials that are thermodynamically unstable.

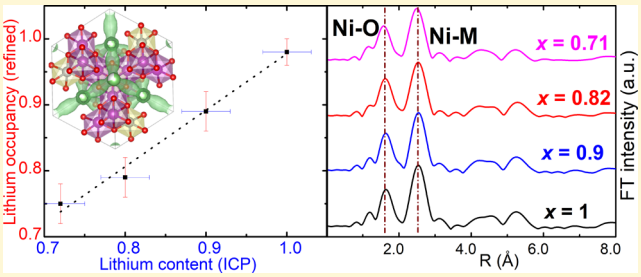

1. INTRODUCTION

The growing market of portable electronics and electric/plug-in hybrid electric vehicles worldwide demands advanced energy storage systems with excellent energy density, cyclability, and thermal stability.[1,2] Among the reported cathode materials, the high-voltage spinel $LiMn_{1.5}Ni_{0.5}O_4$ (LMNO) is of great interest due to its relatively high energy density (700 W h kg^{-1}) and 3D conduction pathways for lithium ions.[3−5] One of its remarkable properties is the structure-dependent redox reaction and phase transformation. The disordered polymorph with an $Fd\bar{3}m$ symmetry, in which Mn and Ni ions are randomly distributed in the 16*d* octahedral sites, is often synthesized at 900 °C through a fast cooling process.[3−5] Kunduraci and others conducted extensive *in situ* powder X-ray diffraction (PXRD) studies and revealed that the disordered spinel has a substantial solid-solution region at low states-of-charge ($Li_xMn_{1.5}Ni_{0.5}O_4$ or L_xMNO, $0.5 < x < 1$).[6,7] The disordered LMNO also possesses higher conductivity largely due to the presence of Mn^{3+}. Both high Mn^{3+} content and the extensive solid-solution involvement are considered to be main reasons behind its superior rate capability, compared to the ordered phase.[8] In the latter case, which has the symmetry of $P4_32_1$, Mn (12*b*) and Ni (4*a*) ions are located in two separate octahedral sites. The ordered LMNO typically has very low Mn^{3+} content, and the Ni cation, whose valence changes from 2+ to 4+ in the two end members, is often the only transition metal involved in the electrochemical reactions.[5] This leads to two consecutive two-phase redox reactions at ~4.7 V (*vs* Li^+/Li) with a much smaller solid-solution region, with the highest reported *x* value L_xMNO approaching 0.8.[9] This value is also morphology-dependent as recently revealed by Hai *et al.*[10] Introducing dopants into the spinel may also alter the solid-solution region. A recent paper by Xiao *et al.* showed that the solid-solution region in $Li_xMn_{1.5}Ni_{0.45}Cr_{0.05}O_4$ with the $P4_32_1$ symmetry was significantly enlarged with Cr doping, which reached $x = \sim 0.4$.[11]

The lattice parameters of the three cubic phases in ordered LMNO, which are LMNO, $L_{0.5}$MNO, and $Mn_{1.5}Ni_{0.5}O_4$ (MNO), were previously determined to be 8.1687(2), 8.0910(6), and 8.0005(3) Å, respectively.[6,10] Recently, advanced 2D and 3D nanotomography was successfully employed to investigate its phase transformation mechanism, but the role of the solid solution remains unclear.[12] The movement of cations in electrode materials, either driven by temperature or voltage, has been well-studied, and the results

Received: May 8, 2017
Revised: July 18, 2017
Published: July 19, 2017

DOI: 10.1021/acs.chemmater.7b01898
Chem. Mater. 2017, 29, 6818−6828

suggest that alternative redox pathways may be promoted through careful manipulation of these movements.[13−15] For example, the existence of a non-equilibrium single-phase electrochemical reaction mechanism was demonstrated in olivine-type $LiFePO_4$ (LFP) under certain conditions, such as fast C-rate (~10 C) charge/discharge, small particle sizes (<50 nm), or samples with large defect concentrations.[16−18] This contrasts with the behavior of conventional micrometer-sized LFP where a typical two-phase redox reaction, consisting of $Li_\alpha FePO_4$ ($L_\alpha FP$) and $Li_{1-\beta}FePO_4$ ($L_{1-\beta}FP$) end members, occurs at 3.5 V (*vs* Li^+/Li).[19] Improvement in kinetics was observed in the former case.

Ordered LMNO resembles LFP in that the two-phase reactions dominate the phase transformation process during Li insertion/extraction. Our previous reports showed that LMNO and $L_{0.5}MNO$ are capable of dissolving into each other at higher temperatures, with the newly formed solid solutions (ss-L_xMNO) maintaining a single phase even after cooling to room temperature.[20] Using operando time-resolved X-ray diffraction, Komatsu *et al.* recently reported the observation of solid-solution domains at the phase transition front during high-rate charging and discharge of LMNO.[21] In this study, we investigated the properties of these non-equilibrium phases and their role during electrochemical charge/discharge of ordered LMNO for the first time. The crystal structure and valence state of the cations were studied by neutron diffraction (ND), soft and hard X-ray absorption spectroscopy (XAS), and bond valence sum (BVS) analysis. *In situ* XRD was used to monitor structural changes during electrochemical Li insertion and extraction. The current study provides an excellent example of probing electrochemical and structural properties of challenging electrode materials that are metastable in nature.

2. EXPERIMENTAL SECTION

2.1. Synthesis. All chemicals were obtained from Aldrich with a purity of 97% or higher. Well-formed octahedral-shaped LMNO crystals were prepared based on our previous reports.[10,20] Varying levels of chemical delithiation were achieved by reacting the pristine oxide powder with 0.1 M nitronium tetrafluoroborate (NO_2BF_4) in acetonitrile solution in an argon-filled glovebox (O_2 <1 ppm and H_2O <1 ppm) at room temperature. The resulting reaction mixtures were filtered, washed with acetonitrile, and dried overnight in a vacuum oven. The lithium contents of the delithiated samples were confirmed by the inductively coupled plasma optical emission spectrometer (ICP-OES; PerkinElmer Optima 5400) analysis.

2.2. Characterization. The cation ratio of the samples was determined by ICP analysis. PXRD patterns were collected using a Panalytical X'Pert Pro diffractometer with monochromatized Cu Kα radiation. The scans were collected between 32 and 80° (2θ) at a rate of 0.0001 deg/s and a step size of 0.022°. Temperature-controlled XRD studies were carried out in the same diffractometer equipped with an Anton Parr HTK 1200 hot stage. The samples were heated in air at a rate of 5 °C/min, and the XRD patterns were recorded at a temperature step size of 25 °C, with each temperature holding for 5 min before data collection. The same procedure was used for the cooling process. Neutron diffraction patterns of LMNO, ss-L_xMNO (x = 0.90, 0.82, and 0.71), and MNO were collected at the POWGEN diffractometer located at the Spallation Neutron Source, Oak Ridge National Laboratory.[22] Two separated banks, with center wavelengths of 1.066 Å (2 h data collection) and 2.665 Å (1 h data collection), were picked to collect the data. Such an arrangement covered a d-spacing range of 0.3−6.2 Å in the autochanger where the temperature was controlled at 300 K. The diffraction data were analyzed by Rietveld refinement in Fullprof Suite.[23] From the refinement, the bond lengths of Ni−O and Mn−O were obtained, which were then used for bond valence sum calculations to estimate the oxidation states of Ni and Mn cations in the samples.[24] Scanning electron microscopy (SEM) images were collected on a JEOL JSM-7500F field emission microscope at a 2 kV accelerating voltage in a gentle beam mode.

For soft XAS measurements, a thin layer of the samples was spread onto a conductive carbon tape which was then attached to an aluminum sample holder inside an Ar-filled glovebox. Measurements were carried out on the 31-pole wiggler beamline 10-1 at Stanford Synchrotron Radiation Lightsource (SSRL) with a ring current of 350 mA, a 1000 l mm^{-1} spherical grating monochromator with 20 mm entrance and exit slits, a 0.2 eV energy resolution, and a 1 mm^2 beam spot. Data were collected at room temperature under ultrahigh vacuum (10^{-9} Torr) in a single load using the Auger electron yield (AEY), total electron yield (TEY), and fluorescence yield (FY) mode detectors. Hard XAS data (Mn and Ni K-edges) were collected in transmission mode using a (220) monochromator at SSRL beamline 4-1. As-prepared and heat-treated L_xMNO powders were dispersed on kapton films for data collection. Higher harmonics in the X-ray beam were reduced by detuning the Si (220) monochromator by 35% at the Ni edge and 50% at the Mn edge. Energy calibration was accomplished by using the first inflection points in the spectra of Ni and Mn metal foil references, which were 8333 and 6539 eV, respectively. Extended X-ray absorption fine structure (EXAFS) data were processed by Sam's Interface for XAS Package or SIXPACK software. Further analysis of EXAFS results was done by using the Demeter software package. Full-field transmission X-ray microscopy (FF-TXM) imaging was performed at the 54-pole wiggler beamline (BL 6-2c) at the SSRL. Detailed beamline configuration can be found in a previous report.[25] Delithiated and solid-solution $Li_{0.71}MNO$ crystals were dispersed in the cylindrical quartz capillary. Slow and steady He gas flow was applied to the crystals to minimize the radiation-induced heat load on the sample during the scans. The X-ray energy was tuned to the Ni K-edge and then focused onto the sample by an elliptically shaped capillary condenser providing illumination for a field of view (FOV) of approximately 30 × 30 μm^2. Two-dimensional transmission images (0.5 s exposure time, 10 repetitions, binning 2, and 1024 × 1024 pixels) were collected from 8100 to 8800 eV in 134 steps for each sample. In order to remove distortions caused by the flux and beam instabilities, concurrent acquisition of reference images at each energy was also performed through an open area of the sample (outside the capillary) with the same imaging configuration. The repetitions in exposures were carried out to enhance the dynamic range of the existing CCD and, subsequently, improve the signal-to-noise ratio in the data. The tomographic reconstruction and data analysis were performed using TXM-Wizard, an in-house-developed software package.

Electronic conductivity measurements were carried out using a two-electrode dc polarization measurement. LMNO and ss-L_xMNO pellets, with diameters of 11 mm and weight of *ca.* 0.2 g each, were prepared by using a pellet press die at a uniaxial force up to 2.4 × 10^7 Pa. The pellets were then sputtered with a thin layer of Au on both sides as blocking electrodes and the measurements were performed over a voltage window of 0.5−2 V, with an increment of 500 mV for each step. The leakage current was recorded as a function of both voltage and temperature.

2.3. Electrochemical Measurements. The composite electrodes were prepared by mixing 80 wt % ss-L_xMNO crystals with 5 wt % SFG-6 synthetic flake graphite (Timcal Ltd., Graphites and Technologies), 5 wt % acetylene carbon black (Denka), and 10 wt % Kynar 2801 poly(vinylidene fluoride) (PVDF) in an *N*-methylpyrrolidone (NMP) solution. The slurry was spread onto aluminum foil and dried overnight at 80 °C under vacuum. The typical electrode loading was 3−4 mg cm^{-2}. Cathode disks with an area of 1.6 cm^2 were cut from the electrode sheets and assembled into 2032-type coin cells in an argon-filled glovebox. Lithium foil (Alfa-Aesar) was used as counter and reference electrodes and Celgard 2400 polypropylene membrane as separators, and 1 M $LiPF_6$ in 1:1 ethylene carbonate (EC):diethylene carbonate (DEC) (Novolyte Technologies Inc.) was used as the electrolytic solution. The cells were galvanostatically cycled in varying voltage windows using a VMP3

DOI: 10.1021/acs.chemmater.7b01898
Chem. Mater. 2017, 29, 6818−6828

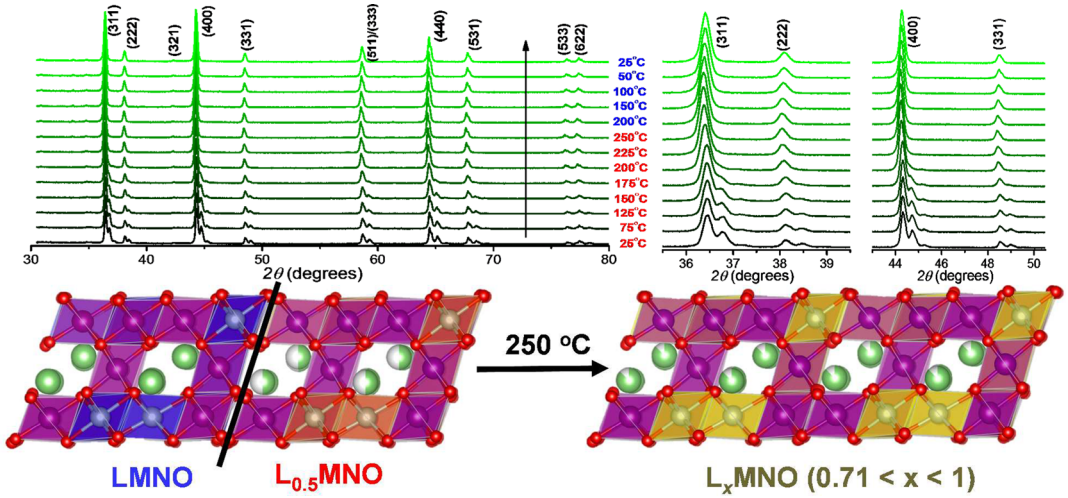

Figure 1. (Top) variable temperature powder XRD patterns of $L_{0.71}$MNO and (bottom) a schematic diagram shows the merge of two phases (LMNO and $L_{0.5}$MNO) into a single-phase ss-L_xMNO ($0.71 < x < 1$) at 250 °C. Green spheres represent Li, purple spheres represent Mn, red spheres represent O, and blue, orange, and yellow spheres represent Ni in LMNO, $L_{0.5}$MNO, and ss-L_xMNO, respectively.

Table 1. Summary of Cell Parameters and Li^+ Occupancy in LMNO, ss-Li_xMNO, and MNO Obtained from Rietveld Refinement of Neutron Diffraction Data

Li occupancy (nominal)	Li occupancy (refined)	a(esd)	B_{iso}(Li)	B_{iso}(Ni)	B_{iso}(Mn)	B_{iso}(O1)	B_{iso}(O2)	R_{wp} (%)	χ^2
1.00	0.98(2)	8.1669(1)	0.4(1)	0.23(2)	0.09(2)	0.16(3)	0.20(2)	4.4	3.3
0.90	0.89(3)	8.1661(1)	0.3(1)	0.30(3)	0.13(3)	0.20(4)	0.23(2)	4.4	2.7
0.82	0.79(3)	8.1667(1)	0.3(2)	0.36(3)	0.20(4)	0.24(4)	0.22(3)	5.2	3.1
0.71	0.75(3)	8.1697(2)	0.7(2)	0.56(3)	0.36(3)	0.44(4)	0.30(2)	8.5	8.4
0	0	7.9995(1)		0.26(1)	0.24(2)	0.32(3)	0.39(1)	5.9	5.0

Table 2. Summary of O Occupancy and Position in LMNO, ss-Li_xMNO, and MNO Obtained from Rietveld Refinement of Neutron Diffraction Data

Li occupancy (nominal)	O (8c) occupancy (nominal/refined)	O (24e) occupancy (nominal/refined)	O (8c) x−y−z position	O (24e) x−y−z position
1.00	1.0/1.01(1)	1.0/1.00(0)	0.3860(2), 0.3860(2), 0.3860(2)	0.1482(2), −0.1412(2), 0.1253(2)
0.90	1.0/1.00(1)	1.0/1.00(1)	0.3863(2), 0.3863(2), 0.3863(2)	0.1478(2), −0.1409(2), 0.1258(2)
0.82	1.0/1.01(1)	1.0/0.995(4)	0.3867(1), 0.3867(1), 0.3867(1)	0.1478(2), −0.1406(2), 0.1258(1)
0.71	1.0/0.99(1)	1.0/0.99(1)	0.3861(1), 0.3861(1), 0.3861(1)	0.1477(1), −0.1411(1), 0.1262(1)
0	1.0/0.99(1)	1.0/0.99(1)	0.3898(2), 0.3898(2), 0.3898(2)	0.1463(2), −0.1287(2), 0.1341(2)

multichannel potentiostat/galvanostat controlled by EC-Lab v10.12 software (BioLogic Science Instruments).

In situ XRD studies were performed at beamline 11-3 at SSRL. Standardized 2032 coin cells were modified with two 3 mm holes at the bottom and top caps (coin cell casing) to allow the penetration of the incident X-ray beam. X-ray transparent kapton tape was used to cover these holes. The entire modified coin cell was then sealed in a polyimide pouch in the glovebox to avoid air and moisture contamination. The XRD patterns were collected every 3 min during galvanostatical charge and discharge at a current density of 10 mA g^{-1}. For ease of data comparison, the 2q scale was converted to angles corresponding to Cu Kα radiation (λ = 1.5406 Å).

3. RESULTS AND DISCUSSION

3.1. Crystal Chemistry of ss-L_xMNO ($0.7 < x < 1$). The pristine LMNO sample prepared by the molten-salt method was octahedron-shaped crystals about 2 μm in average size dominated by the (111) family of facets on the surface.[10] A series of delithiated L_xMNO samples ($0 \leq x < 1$) were prepared by the chemical oxidation method, and their lithium contents were confirmed by ICP analysis. The thermally driven structural changes in L_xMNO were then monitored by variable temperature powder X-ray diffraction (VT-PXRD), with the temperature ranging from 25 to 250 °C at an increment step size of 25 °C. Figure 1 shows the XRD patterns of $L_{0.71}$MNO as a function of temperature, with the expanded regions of 35.5−39.5° and 43−50.5° (2θ) also shown on the right. The presence of LMNO and $L_{0.5}$MNO which have the same spinel structure but slightly different cell parameters can be easily identified by the two sets of diffraction peaks at close 2θ values. As the temperature increased, the pairs of peaks started to merge with each other which eventually became a single set at 250 °C. This confirms the formation of a single-phase solid-solution $L_{0.71}$MNO (ss-$L_{0.71}$MNO). The solid solution persisted upon cooling, and it was found to be stable even after long-term storage at room temperature or soaking in 1.0 M $LiPF_6$ in ethylene carbonate (EC) and diethylene carbonate (DEC; 1:1 (v/v)) electrolyte for an extended period, or even aggressive grinding, as shown by the XRD pattern comparison in Supporting Information Figure S1. Similar behavior was observed on two other solid-solution samples that were investigated, and single-phase ss-$L_{0.82}$MNO and ss-$L_{0.9}$MNO were obtained at 200 and 225 °C, respectively. Due to the

DOI: 10.1021/acs.chemmater.7b01898
Chem. Mater. 2017, 29, 6818−6828

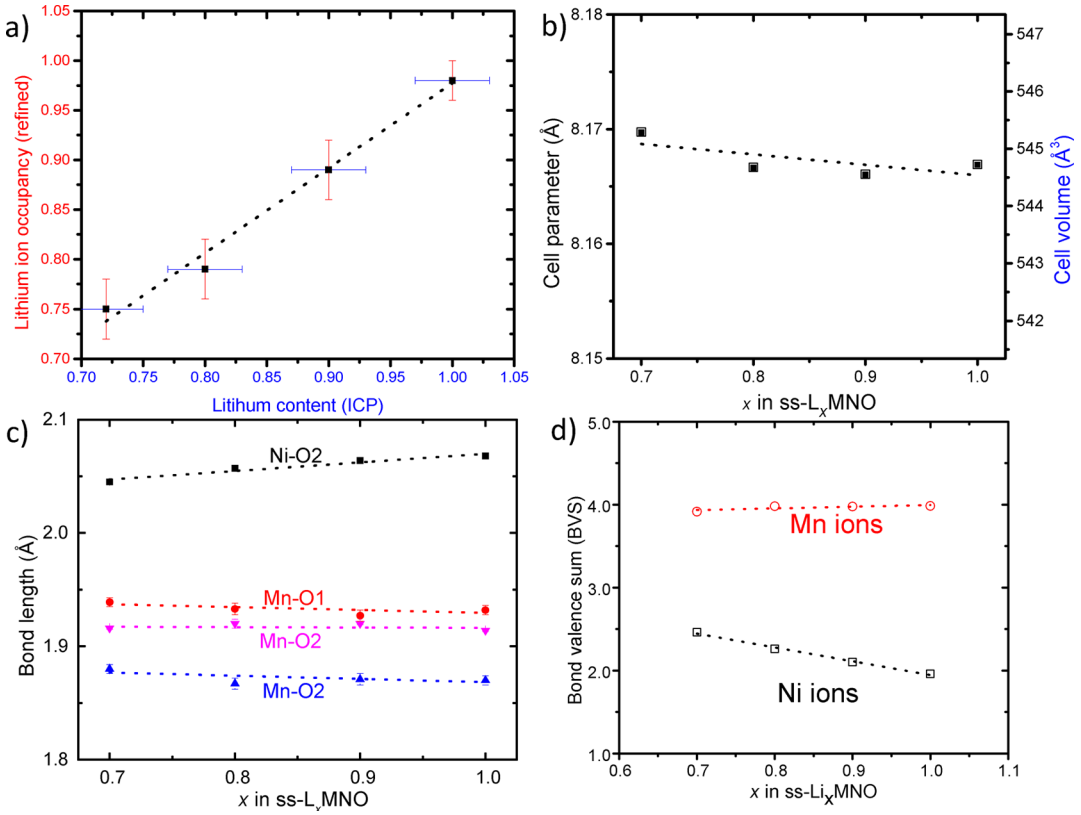

Figure 2. (a) Relationship between the lithium content obtained by Rietveld refinement of neutron diffraction data and by ICP measurements, (b) lattice parameter and cell volume as a function of lithium content x in ss-L_xMNO, (c) changes in Ni−O and Mn−O bond length as a function of x in ss-L_xMNO, and (d) bond valence sum analysis as a function of x in ss-L_xMNO.

coarseness of the chemical delithiation step size and the large gap in Li content among the samples, the Li content range in the solid solution could only be estimated, and ranges from 0.7 < x < 1. The details on the L_xMNO phase diagram were reported in a previous publication.[20]

In a true spinel solid solution, all lithium ions are expected to reside in the tetrahedral 8*c* sites. A linear correlation between the overall lithium content in the sample (determined by elemental analysis such as ICP-OES) and the structurally refined lithium ion occupancy can be expected. Experimentally, structural analysis is best achieved by neutron diffraction as the neutron scattering length provides a better contrast in differentiating lithium and other transition metal cations in LMNO (*i.e.*, Li = −1.9 *vs* Mn = −3.73 and Ni = 10.3) than its X-ray analogue (*i.e.*, Li = 3.92 *vs* Mn = 55.37 and Ni = 64.41).[26] Previous neutron diffraction studies have been performed on pristine LMNO, which revealed that the superstructure reflections are often broader than the underlying $Fd\bar{3}m$ reflections. This is due to the smaller size of ordering domains controlled by the solid-state synthesis conditions.[27,28] Figure S2, Table 1, and Table 2 show the results from the Rietveld refinement of neutron diffraction patterns of the pristine LMNO and ss-L_xMNO (0.71 < x < 1). It is evident that the pristine LMNO crystals are phase-pure with a well-ordered spinel structure (space group $P4_32_12$), although slight broadening in the superstructure peaks was also observed. The ordered spinel structure is maintained in all the solid-solution phases, with Li, Mn, and Ni atoms located at 8*c*, 4*a*, and 12*d*, respectively. A linear relationship between the analyzed and the refined lithium content was indeed observed (Figure 2a), confirming that lithium ions in the samples are located exclusively on 8*c* sites. Figure 2b shows the changes in lattice parameter as a function of x. Reducing the Li content leads to larger-sized lithium ion vacancies, smaller-sized NiO_6 octahedra, and similar-sized MnO_6 octahedra in the structure, which results in nearly constant lattice parameters and cell volumes in the series of compositions. Figure 2c shows the changes in Mn−O and Ni−O bond lengths obtained from the Fullprof Suite analysis.[23] In spinel LMNO, both O1 and O2 are in tetrahedral coordination but they have quite different environments. O1 is coordinated with three Mn cations (all at a bond length of 1.93 Å) and one Li cation (also at a bond length of 1.93 Å). O2 is in a distorted tetrahedral environment as it is coordinated with metal cations with different valence states. O2 directly bonds with two Mn cations (at bond lengths of 1.87 and 1.91 Å, respectively), one Ni cation (at a bond length of 2.068 Å), and one Li cation (at a bond length of 1.96 Å). With decreasing Li content in ss-L_xMNO, the Ni−O2 bond length decreases from 2.068 to 2.045 Å in ss-$Li_{0.71}$MNO. On the other hand, Mn−O bonds remain nearly constant, with Mn−O1 bond length at ∼1.93 Å and Mn−O2 bonds at ∼1.87 and ∼1.91 Å in all ss-L_xMNO (0.71 ≤ x < 1) samples.

Oxygen vacancy is traditionally estimated by iodometry which determines the average oxidation state of the transition metals. We recently investigated the changes in the oxidation state of Ni and Mn in the spinel samples by using hard XAS which has been widely used to determine the chemical state of transition metals.[20] The results showed negligible oxygen vacancy in ss-L_xMNO, as both transition metals have the same oxidation state expected from charge neutrality. The valence states of Mn and Ni in the bulk of LMNO and ss-L_xMNO were also estimated by the bond valence sum method, an empirical

DOI: 10.1021/acs.chemmater.7b01898
Chem. Mater. 2017, 29, 6818−6828

Table 3. Summary of M−O Bond Lengths and Bond Valences of M in LMNO, ss-Li$_x$MNO, and MNO, Where M = Mn and Ni

Li occupancy (nominal)	Ni−O2 (×6)	bond valence sum (Ni)	Mn−O1 (×2)	Mn−O2 (×2)	Mn−O2 (×2)	bond valence sum (Mn)
1.00	2.068(2)	1.96(1)	1.932(4)	1.870(4)	1.914(1)	3.99(1)
0.90	2.064(2)	2.10(1)	1.927(5)	1.871(5)	1.920(1)	3.98(1)
0.80	2.057(2)	2.26(1)	1.933(5)	1.867(5)	1.920(1)	3.98(1)
0.72	2.045(2)	2.46(2)	1.939(4)	1.880(4)	1.916(4)	3.92(1)
0	1.888(1)	3.79(1)	1.906(4)	1.911(3)	1.908(1)	3.94(1)

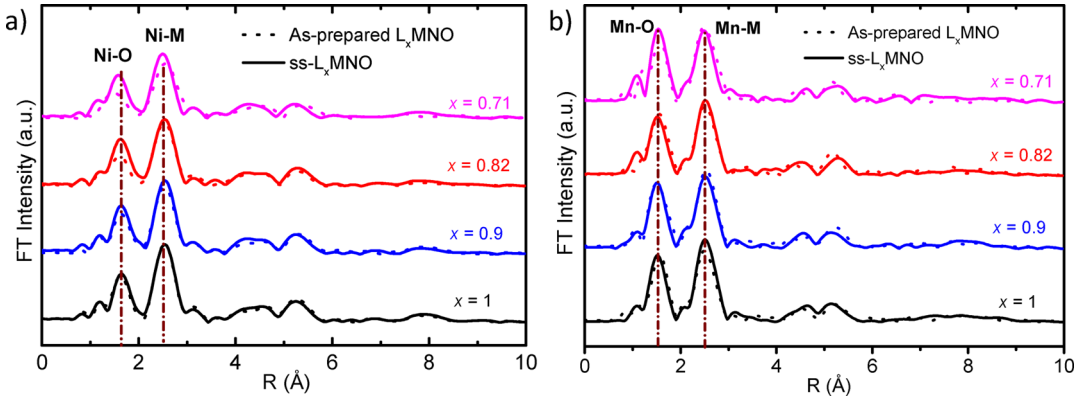

Figure 3. Fourier-transformed (a) Ni K-edge and (b) Mn K-edge EXAFS spectra showing metal−oxygen and metal−metal bond distances in the as-prepared and solid-solution L$_x$MNO samples.

approach that correlates the bond valence and the bond length. The relationship can be expressed in the following equation:

$$S = \sum s_i; \quad s_i = \exp(R_o - R)/b \tag{1}$$

where S, s_i, R_o, R, and b are the total valence, bond valence, reference bond length, bond length, and 0.37, respectively.[24] As shown in both Table 3 and Figure 2d, the valence state of Mn ions was found to be constant at 4+ while the valence state of Ni cations increased continuously from 2+ in LMNO to 2.46+ in ss-Li$_{0.71}$MNO as lithium content decreased, consistent with the previous literature report showing that only nickel ions are involved in the redox reduction of L$_x$MNO.[5] The BVS calculation further confirms that oxygen vacancies do not exist in the solid-solution samples. Moreover, when the O1 and O2 occupancies were allowed to refine in the neutron refinement, they did not move within estimated errors of unity. These studies led us to conclude that negligible defects exist in the ss-L$_x$MNO solid-solution samples.

The local environment around Mn and Ni cations was evaluated by PDF analysis of Fourier-transformed extended X-ray absorption fine structure (EXAFS) spectra, obtained from the hard X-ray absorption measurements at SSRL. The k^3-weighted K-edge spectra of ss-L$_x$MNO samples were compared with the corresponding as-prepared L$_x$MNO samples prior to the heat treatment, and the results are shown in Figure 3. While Figure 3a shows that the Ni−O bond length gradually decreases along with the decrease of the Li content in ss-L$_x$MNO, the Mn−O bond length is nearly constant in all solid-solution samples (Figure 3b). This is consistent with the results from the neutron refinement, further confirming the inert nature of Mn^{4+} ions whose local environment (bond length and coordination number) in ordered L$_x$MNO is largely unaltered. Note that since the spectra are not phase corrected, the bond lengths in the PDF spectra are in general 0.2−0.4 Å shorter than the actual values.

The chemical homogeneity of the particles was further investigated by soft XAS, which directly probes the changes in valence state of Ni and Mn as a function of the depth of penetration, a vital tool for understanding variations in oxidation states. The depth profiling from the surface to bulk can be achieved by using three different detectors in Auger electron yield (AEY), total electron yield (TEY), and fluorescence yield (FY) modes, which have a typical probing depth of 2, 5, and 50 nm, respectively.[29] The measured L$_{III}$-edges ($2p_{3/2} \rightarrow 3d$) of Ni and Mn are centered at 852.6 and 643.6 eV, respectively, both of which have a line splitting feature resulting from the core hole spin−orbital coupling.[30] As shown in the Ni FY spectra in Figure 4a, the relative area of Ni L$_{III,\alpha}$ (~852 eV) to L$_{III,\beta}$ (~854.5 eV) decreases with decreasing lithium content in the as-prepared L$_x$MNO, corresponding to an increase in the fraction of the L$_{0.5}$MNO with a higher Ni cation valence. Similar values were obtained from the TEY spectra (Figure 4b), while the slightly lower values obtained in the AEY mode (Figure 4c) suggest that some Ni reduction may have occurred on the very top surface of less than 2 nm on the particles. In the ss-L$_x$MNO series, the bulk Ni shows a slightly higher oxidation state compared to that in the as-prepared counterpart. Both TEY and AEY spectra, however, show a Ni oxidation state of 2+, which is the same as in LMNO (Figure 4e). This indicates the presence of a surface reduction layer of at least 5 nm, which is much thicker than that in the as-prepared counterpart. It appears that, during the heat treatment, Ni was further reduced to a lower oxidation state which progressed from the surface toward the bulk. The formation of such a thin surface layer is not uncommon in metal oxides and is often attributed to the lower oxygen atom coordination number around the cations on the surface.[31,32] In the case of ss-L$_x$MNO, the formation of a surface reduction layer may also be related to oxygen loss during the heat treatment. For the Mn L$_{III}$-edge, the relative area of Mn L$_{III,\beta}$ (~643.6 eV) to L$_{III,\alpha}$ (~654.0 eV) in FY mode remains unchanged with decreasing lithium content (Figure 4d), confirming that the valence state of Mn stays at 4+ in all

DOI: 10.1021/acs.chemmater.7b01898
Chem. Mater. 2017, 29, 6818−6828

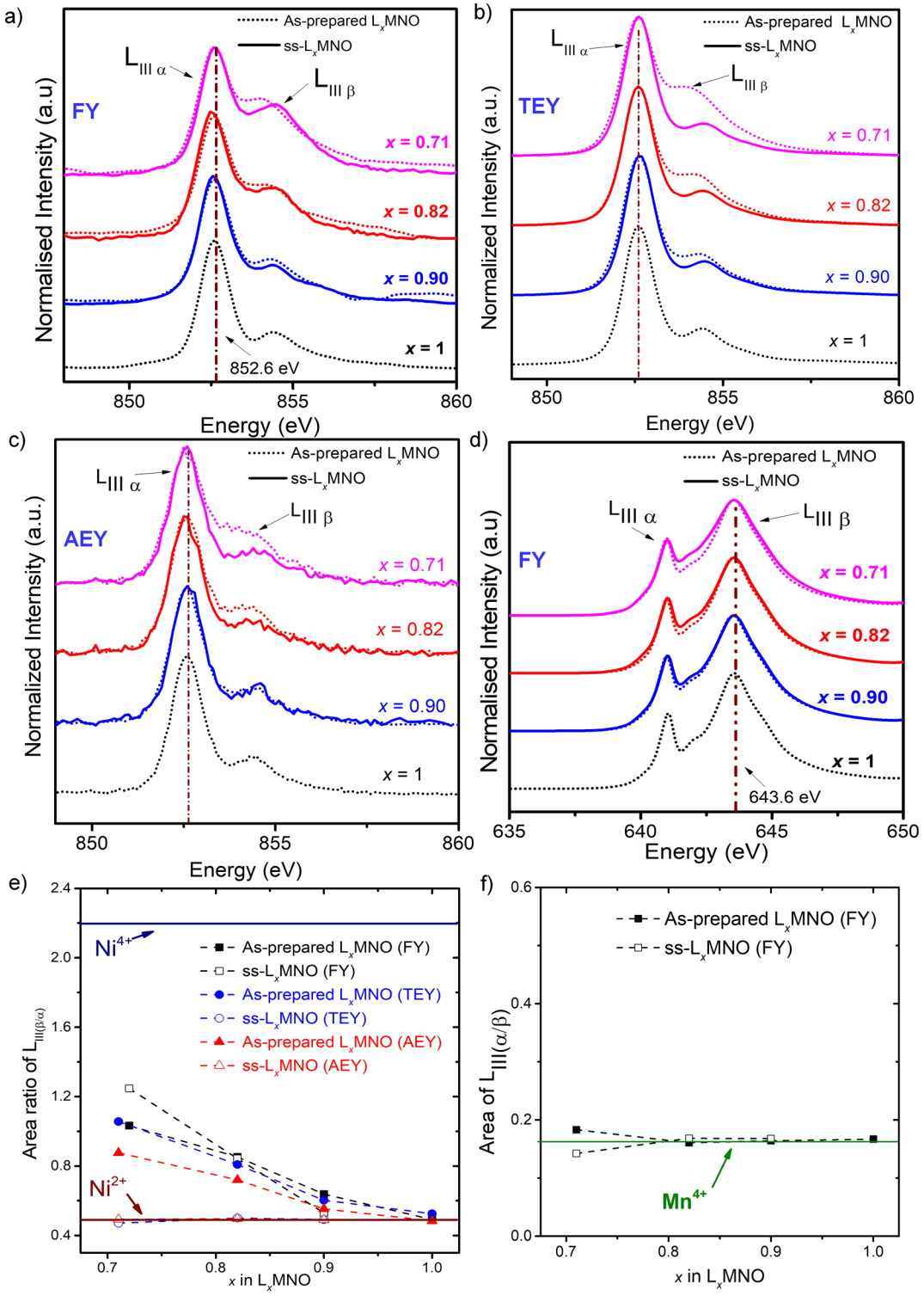

Figure 4. Soft XAS Ni L-edge spectra in (a) FY, (b) TEY, and (c) AEY modes; (d) soft XAS Mn L-edge spectra in FY mode; (e and f) relative ratio of $L_{III,\beta}/L_{III,\alpha}$ for Ni and Mn ions, respectively, in both as-prepared and solid-solution L_xMNO samples.

samples and it is insensitive to the change of lithium content (Figure 4f).

The presence of lithium ion vacancies and mixed Ni cation valence states in ss-L_xMNO are likely to impact the lithium ion and/or electron transport properties. To this end, we performed conductivity measurements on the pristine LMNO and the ss-L_xMNO series samples with a two-electrode dc polarization apparatus. To avoid the possibility of thermal decomposition, the samples were pelletized anisotropically with an applied pressure up to 2.4×10^7 Pa without sintering. The calculated pellet porosity, based on the weight (0.2 g), dimension (11 mm in diameter and 0.7 mm in thickness), and density of the spinel oxide (4.27 g/cm^3), was only about 70%. Consequently, the apparent resistance may be over-estimated due to the contribution of ohmic resistance from the grain boundaries. An estimated additional 5% error range can

DOI: 10.1021/acs.chemmater.7b01898
Chem. Mater. 2017, 29, 6818−6828

also be expected from instrumental limitations. Nonetheless, all samples were prepared in the same manner and a qualitative comparison within the series still provides insights on the electrical properties. As shown in Figure 5, the activation

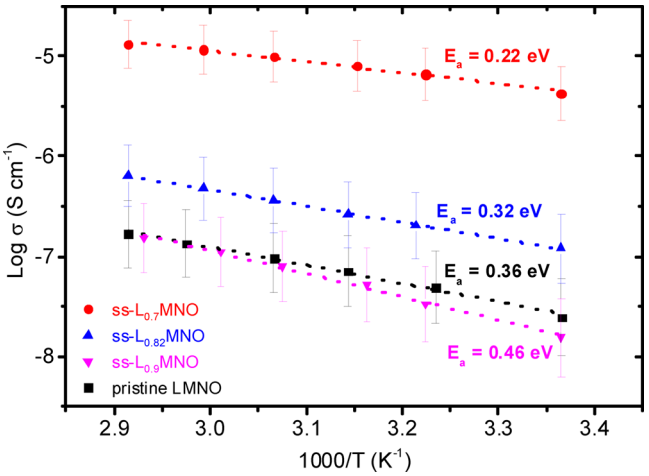

Figure 5. Electric conductivities of pristine LMNO and ss-L_xMNO measured by the two-probe apparatus. Error bars of ±5% were estimated for instrumental error.

energies were found to decrease with decreasing lithium content, consistent with the trend of increasing Li vacancy concentration and Ni^{2+} and Ni^{3+} ion mixing in the samples. The conductivity of ss-$Li_{0.71}$MNO was found to be the highest among all investigated samples, at least two orders of magnitude higher compared to that of the pristine LMNO at room temperature.

Lithium ion transport properties were further evaluated by using BVS maps which were calculated by assigning the oxidation state and occupancy of all atoms in the crystallography information files (CIF) based on the results from the ICP-OES analysis.[33] This provides spatial distribution of valence values on the 3D unit cells visually, with the well-connected low bond valence mismatch isosurface considered as a low-energy pathway in the space. This simple methodology has been used to calculate bond valences in various electrode and electrolyte materials and has been found to agree well with the maximum entropy method (MEM) of neutron diffraction data.[34] Figure 6 shows the 3D conduction pathways for lithium ions projected on the highly symmetric (100), (110), and (111) planes. In all cases, the topology is similar to other spinels with mixed valence such as LiM_2O_4 (M = Ti, Mn),[35] suggesting that the 3D lithium ion pathways are not sensitive to the redistribution of Ni valences. However, given the fact that more lithium ion vacancies exist in the solid solutions, the diffusivity of the lithium ions can be expected to be higher in the metastable ss-L_xMNO phases than that in pristine LMNO.

3.2. Electrochemistry of ss-L_xMNO. *In situ* XRD measurements of half-cells containing ss-L_xMNO crystal composite electrodes were performed at SSRL beamline 4-1, and the results on ss-$L_{0.82}$MNO are shown in Figures 7 and 8. The open circuit voltage (OCV) was measured to be ~3.7 V *vs* Li^+/Li, significantly lower compared to the equilibrium potential of ~4.7 V. This may be due to the fact that there is a surface layer with reduced Ni on the particles, as evidenced by the soft XAS studies. Upon the initial first charge to 4.8 V, only about 0.19 Li^+ was extracted from $Li_{0.82}Mn_{1.5}Ni_{0.5}O_4$ (Figure 7a), suggesting the effect of large polarization, likely due to the presence of the reduced surface layer. A single solid-solution phase with Li content of $0.63 \leq x < 0.82$, determined by coulometry, was maintained during the charging process (Figure 7b). This corresponds to a solubility of *ca.* 1:3 between $L_{0.5}$MNO and LMNO. Note that the minimum Li content in the solid solution ($x \geq 0.63$) is lower compared to what was determined from the thermal study, which was $x > 0.7$. Aside from the fact that different preparation methods may lead to the formation of different metastable phases, another possible source for this discrepancy is the contributions from side reactions to the coulometry which leads to overestimation of the Li content in the solid solution. For the subsequent (first) discharge, only 0.09 Li^+ was reinserted into the compound to a lower cutoff voltage of 4.2 V, corresponding to $x = 0.72$ in ss-L_xMNO. This further indicates the significant role of the surface reduced layer on the electrochemical behavior of the sample. No detectable structural changes were observed in the XRD patterns between 4.2 and 4.8 V (Figure 7b). On the second charge to 4.8 V, about 0.27 Li^+ was removed, which corresponds to $x = 0.45$ in L_xMNO. A second set of peaks, labeled (331)′, (511)′, and (531)′ in Figure 7c, appeared when the Li content was below ~0.64, consistent with the determined solubility limit of *ca.* 1:3 between $L_{0.5}$MNO and LMNO. The new set of peaks correspond to the $L_{0.5}$MNO phase with a lattice parameter of 8.097 Å. Upon discharge to 4.2 V, $L_{0.5}$MNO disappeared around a Li content of ~0.62. At the end of discharge at 4.2 V, the spinel solid-solution ss-$Li_{0.65}$MNO with a lattice parameter of 8.167 Å became the only

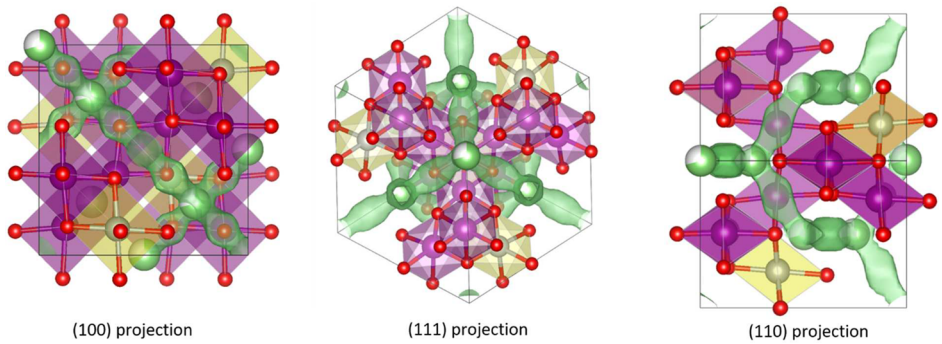

Figure 6. Lithium migration pathways projected on (100), (111), and (110) planes in ss-$L_{0.71}$MNO. Purple spheres represent Mn, red spheres represent O, yellow spheres represent Ni, and green spheres represent Li. Calculated low bond valence mismatch pathways for lithium ions are also shown in green on the contour surface.

DOI: 10.1021/acs.chemmater.7b01898
Chem. Mater. 2017, 29, 6818−6828

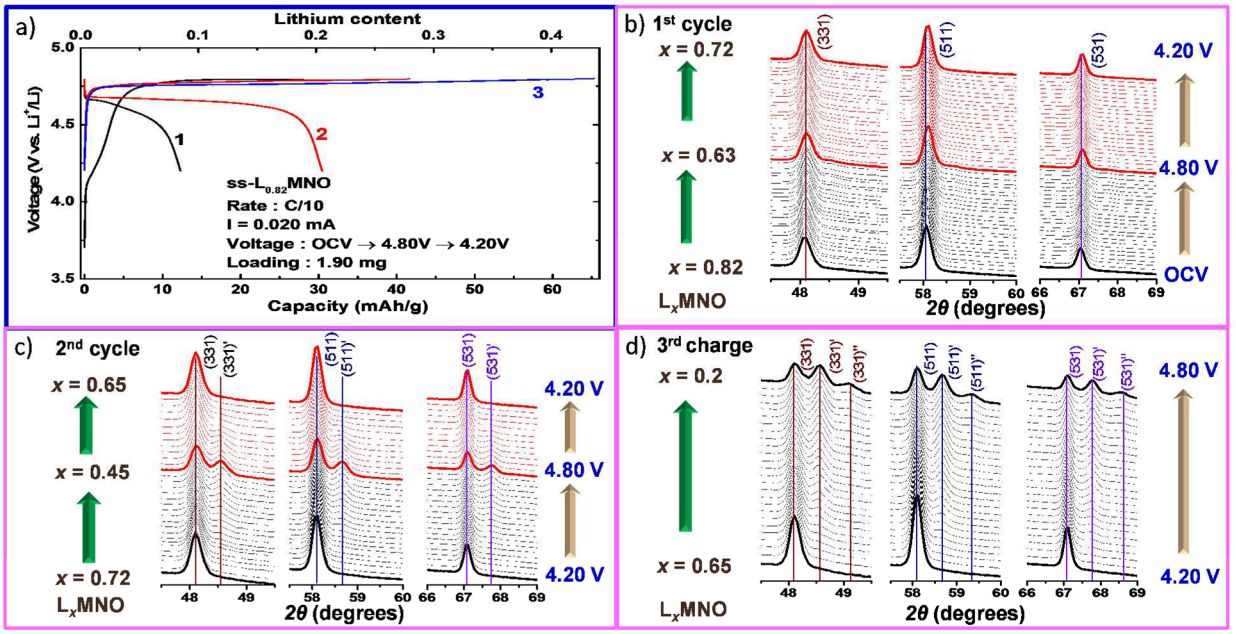

Figure 7. (a) Charge/discharge voltage profiles of ss-$L_{0.82}$MNO and (b–d) the corresponding X-ray diffraction patterns collected from the *in situ* half-cells.

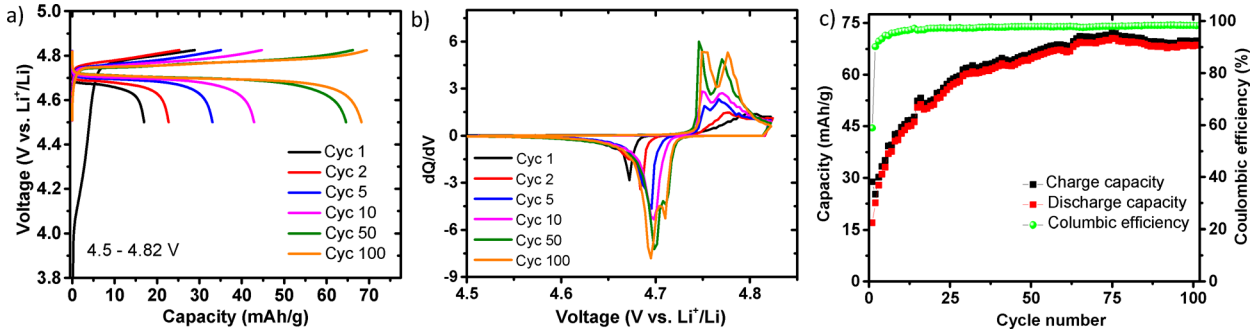

Figure 8. (a) Charge/discharge voltage profiles, (b) dQ/dV profiles, and (c) long-term cycling performance of a ss-$L_{0.82}$MNO half-cell.

phase. On the third charge to 4.8 V (Figure 7d), $L_{0.5}$MNO appeared at x = ~0.6 which was followed by the appearance of fully delithiated MNO at x = ~0.2 (diffraction peaks labeled (331)″, (511)″, and (531)″). Figure 8 shows the voltage profiles, incremental capacity profiles, and capacity retention during the first 100 cycles of ss-$L_{0.82}$MNO between 4.5 and 4.82 V. A gradual increase in capacity with cycling was observed, reaching a value of 70 mA h/g at the 100th cycle (Figure 8a). This is likely due to a reduction in surface polarization and improved material utilization upon continuous cycling. The single-phase behavior was only maintained during the first two cycles, as evidenced by the single peaks on the incremental capacity profiles (Figure 8b). Phase separation, signaled by the doublet at 4.75 and 4.78 V in the profile, was observed on the third cycle, where more Li^+ was extracted and inserted compared to the previous two cycles. This is consistent with the observation that the solid-solution behavior can only be maintained in the lithium content range of ~0.6 < x < 1. When charge and discharge occur outside this window (starting at the third cycle), the electrochemical behavior is similar to what was observed in LMNO where single-phase behavior dominates in the lithium content range of ~0.6 < x < 1 followed by the two-phase behavior. The details in structural evolution during charge and discahrge of LMNO was reported in a previous publicatioin.[10] The study clearly reveals the dominating effect of LMNO and $L_{0.5}$MNO solubility in the phase transformation process. Both capacity and coulombic efficiency were found to increase with cycle number (Figure 8c), consistent with lowered polarization and improved material utilization upon continuous cycling. Similar behavior was also observed with ss-$L_{0.71}$MNO.

3.3. Metastability in ss-L_xMNO. These combined thermal and electrochemical studies have shown that $Li_xMn_{1.5}Ni_{0.5}O_4$ solid solutions can exist in the Li content range of ~0.65 < x < 1. We previously showed that the solid solution appeared as a transient phase during electrochemical charge/discharge of LMNO and phase separates upon the removal of current.[20] The thermally driven solid solution, however, can be isolated and maintained at room temperature for a long period of time. Recently, Kishida *et al.* performed a thermodynamic analysis of L_xMNO ($0 \le x \le 1$), and their calculations showed that x = 0, 0.5, and 1 are the most stable phases in the system at 0 K, consistent with the experimental detection of the three phases during Li extraction and insertion of LMNO.[36] However, their decomposition energy was comparable to that of other compositions, with a difference as small as ~0.4 eV calculated. This indicates that less stable L_xMNO phases may easily form under external stimulus. The successful synthesis of ss-L_xMNO

DOI: 10.1021/acs.chemmater.7b01898
Chem. Mater. 2017, 29, 6818–6828

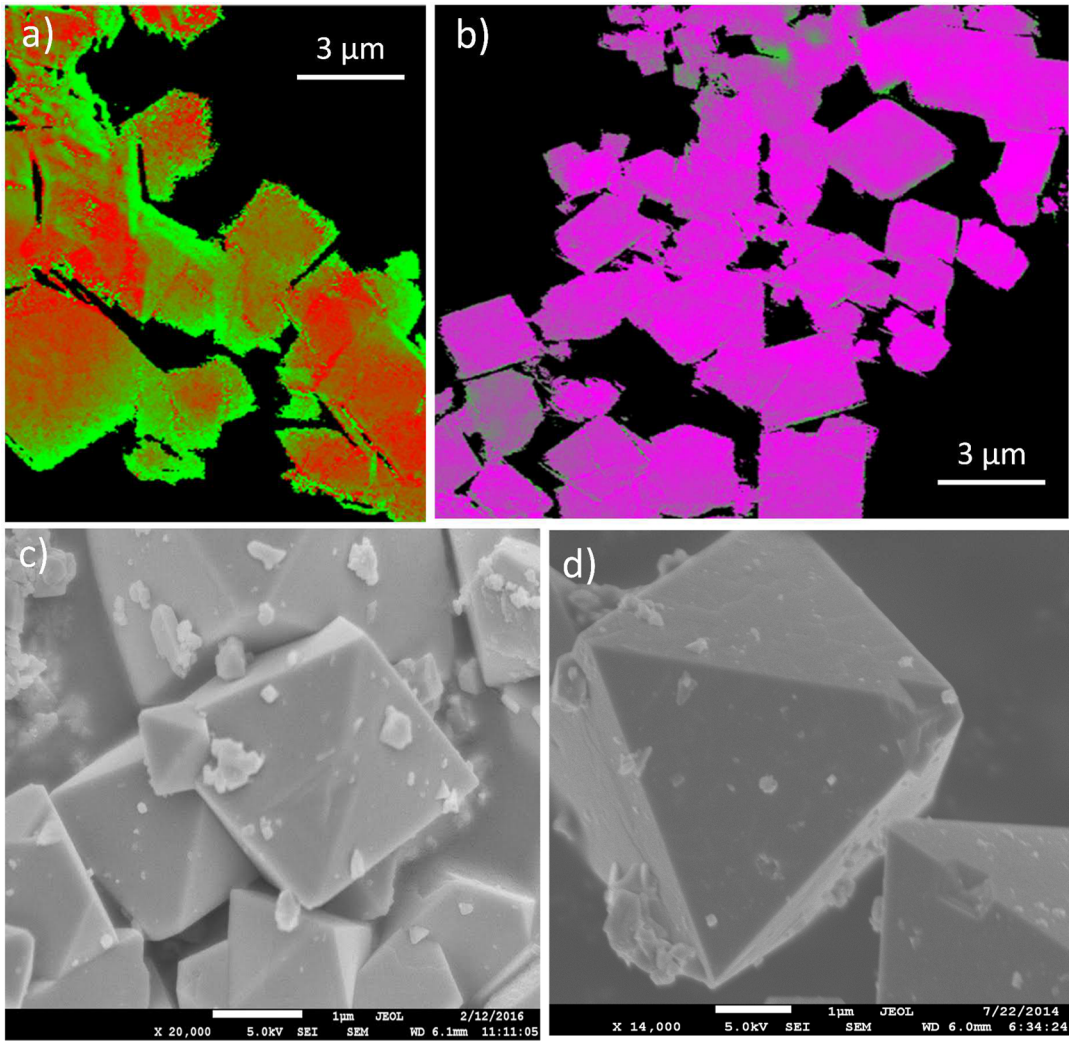

Figure 9. (a and b) TXM Ni oxidation-state maps of the as-prepared and solid-solution $L_{0.71}$MNO crystals and (c and d) SEM images of the as-prepared and solid-solution $L_{0.82}$MNO crystals.

solid solutions at elevated temperatures clearly supports this conclusion. Panels a and b of Figure 9a show the distribution of Ni oxidation states in the as-prepared $L_{0.71}$MNO and ss-$L_{0.71}$MNO, respectively, constructed from single-pixel TXM-XANES spectra (at a spatial resolution of 30 nm) collected at SSRL. While phase segregation is clearly seen in the as-prepared sample, a homogeneous Ni oxidation state in the entire particle of ss-$L_{0.71}$MNO suggests that thermally driven Li movement occurs at the particle level. Although ss-Li_xMNO bears much similarity to Li_xFePO_4 solid solutions, it is significantly more stable. Considering that the Li mobility in LMNO is generally higher, mostly due to the presence of 3D Li diffusion pathways in the cubic lattice, we speculate that the enhanced stability is related to the small enthalpy difference among the phases in the LMNO system. The presence of the surface reduction layer may also play a role in preventing phase separation in the formed solid solutions. As shown in the SEM images in Figure 9c, pitting and other surface roughing features were broadly observed in the solid-solution particles, suggesting that during the thermal treatment, mass changes such as oxygen loss may have occurred along with the reduction of Ni on the surface. The presence of this reduced layer also contributes to the observed polarization during the cycling of ss-Li_xMNO electrodes. Detailed properties of the surface layer are currently being investigated and will be reported in the future.

4. CONCLUSIONS

The role of non-equilibrium single-phase redox reaction in the performance of intercalation electrode materials was revealed through the studies performed on a series of Li_xMNO ($0.71 < x < 1$) solid-solution phases in the ordered high-voltage spinel. Formation of solid solution is observed in the Li content range of $\sim 0.65 < x < 1$ which is promoted either through thermal treatment or electrochemical Li insertion/extraction of pre-synthesized ss-Li_xMNO. The observation of phase segregation outside of this window reveals the solubility limit of *ca.* 1:3 between $L_{0.5}$MNO and LMNO. Detailed analysis on the crystal structure and valence state of the transition metal cations in ss-L_xMNO are presented for the first time. While XAS and BVS studies confirmed that Ni is the only redox active transition metal, ND patterns revealed a substantial amount of lithium ion vacancies in the solid-solution phases, a key feature that enables the single-phase redox process at low state-of-charge evidenced by *in situ* XRD studies. BVS mapping also reveals low-energy 3D topological pathways for lithium ion transport, supporting the observed higher conductivity in ss-L_xMNO. Our findings provide insights and guidance on the synthesis of difficult

DOI: 10.1021/acs.chemmater.7b01898
Chem. Mater. 2017, 29, 6818−6828

metastable phases and their investigation as potential electrode materials for rechargeable lithium or sodium batteries.

■ ASSOCIATED CONTENT

Supporting Information

The Supporting Information is available free of charge on the ACS Publications website at DOI: 10.1021/acs.chemmater.7b01898.

PXRD patterns of solid-solution samples before and after a treatment and Rietveld refinement of neutron diffraction patterns (PDF)

■ AUTHOR INFORMATION

Corresponding Author

*E-mail: gchen@lbl.gov.

ORCID

Jagjit Nanda: 0000-0002-6875-0057

Guoying Chen: 0000-0002-3218-2609

Author Contributions

‖W.H.K. and S.K. contributed equally to this work.

Notes

The authors declare no competing financial interest.

■ ACKNOWLEDGMENTS

We thank Drs. Young-Sang Yu, Yijin Liu, Dennis Nordlund and Tim Dunn for helping with the experiments carried out at SSRL. Use of the Stanford Synchrotron Radiation Lightsource, SLAC National Accelerator Laboratory, is supported by the U.S. Department of Energy, Office of Science, Office of Basic Energy Sciences under Contract No. DE-AC02-76SF00515. We thank Dr. Chetan Dhital for help with the neutron diffraction measurements. The POWGEN beamline at the Oak Ridge National Laboratory's (ORNL) Spallation Neutron Source (SNS) is sponsored by the Scientific User Facilities Division, Office of Basic Energy Sciences, U.S. Department of Energy. This work was supported by the Assistant Secretary for Energy Efficiency and Renewable Energy, Office of FreedomCAR and Vehicle Technologies of the U.S. Department of Energy under Contract No. DE-AC02-05CH11231.

■ REFERENCES

(1) Goodenough, J. B.; Manthiram, A. A perspective on electrical energy storage. *MRS Commun.* **2014**, *4*, 135−142.

(2) Manthiram, A. Materials Challenges and Opportunities of Lithium Ion Batteries. *J. Phys. Chem. Lett.* **2011**, *2*, 176−184.

(3) Liu, G. Q.; Wen, L.; Liu, Y. M. Spinel $LiNi_{0.5}Mn_{1.5}O_4$ and its derivatives as cathodes for high-voltage Li-ion batteries. *J. Solid State Electrochem.* **2010**, *14*, 2191−2202.

(4) Santhanam, R.; Rambabu, B. Research progress in high voltage spinel $LiNi_{0.5}Mn_{1.5}O_4$ material. *J. Power Sources* **2010**, *195*, 5442−5451.

(5) Manthiram, A.; Chemelewski, K.; Lee, E.-S. A perspective on the high-voltage $LiMn_{1.5}Ni_{0.5}O_4$ spinel cathode for lithium-ion batteries. *Energy Environ. Sci.* **2014**, *7*, 1339−1350.

(6) Kunduraci, M.; Amatucci, G. G. Synthesis and Characterization of Nanostructured 4.7 V $Li_xMn_{1.5}Ni_{0.5}O_4$ Spinels for High-Power Lithium-Ion Batteries. *J. Electrochem. Soc.* **2006**, *153*, A1345−A1352.

(7) Rhodes, K.; Meisner, R.; Kim, Y.-G.; Dudney, N.; Daniel, C. Evolution of Phase Transformation Behavior in $Li(Mn_{1.5}Ni_{0.5})O_4$ Cathodes Studied By In Situ XRD. *J. Electrochem. Soc.* **2011**, *158*, A890−A897.

(8) Zheng, J.; et al. Enhanced Li^+ ion transport in $LiNi_{0.5}Mn_{1.5}O_4$ through control of site disorder. *Phys. Chem. Chem. Phys.* **2012**, *14*, 13515−13521.

(9) Ariyoshi, K.; Iwakoshi, Y.; Nakayama, N.; Ohzuku, T. Topotactic Two-Phase Reactions of $Li[Ni_{1/2}Mn_{3/2}]O_4$ ($P4_332$) in Nonaqueous Lithium Cells. *J. Electrochem. Soc.* **2004**, *151*, A296−A303.

(10) Hai, B.; Shukla, A. K.; Duncan, H.; Chen, G. The effect of particle surface facets on the kinetic properties of $LiMn_{1.5}Ni_{0.5}O_4$ cathode materials. *J. Mater. Chem. A* **2013**, *1*, 759−769.

(11) Xiao, J.; Yu, X.; Zheng, J.; Zhou, Y.; Gao, F.; Chen, X.; Bai, J.; Yang, X.-Q.; Zhang, J.-G. Interplay between two-phase and solid solution reactions in high voltage spinel cathode material for lithium ion batteries. *J. Power Sources* **2013**, *242*, 736−741.

(12) Kuppan, S.; Xu, Y.; Liu, Y.; Chen, G. Phase Transformation Mechanism in $LiMn_{1.5}Ni_{0.5}O_4$ Cathode Particles Revealed by Single-Crystal Hard X-ray Microscopy. *Nat. Commun.* **2017**, *8*, 14309.

(13) Kan, W. H.; Huq, A.; Manthiram, A. Exploration of a Metastable Normal Spinel Phase Diagram for the Quaternary Li-Ni-Mn-Co-O System. *Chem. Mater.* **2016**, *28*, 1832−1837.

(14) Kan, W. H.; Huq, A.; Manthiram, A. Low-Temperature Synthesis, Structural Characterization, and Electrochemistry of Ni-Rich Spinel-like $LiNi_{2-y}Mn_yO_4$ ($0.4 \leq y \leq 1$). *Chem. Mater.* **2015**, *27*, 7729−7733.

(15) Delacourt, C.; Poizot, P.; Tarascon, J.-M.; Masquelier, C. The existence of a temperature-driven solid solution in Li_xFePO_4 for $0 \leq x \leq 1$. *Nat. Mater.* **2005**, *4*, 254−260.

(16) Gibot, P.; Casas-Cabanas, M.; Laffont, L.; Levasseur, S.; Carlach, P.; Hamelet, S.; Tarascon, J.-M.; Masquelier, C. Room-temperature single-phase Li insertion/extraction in nanoscale Li_xFePO_4. *Nat. Mater.* **2008**, *7*, 741−747.

(17) Li, Y.; et al. Current-induced transition from particle-by-particle to concurrent intercalation in phase-separating battery electrodes. *Nat. Mater.* **2014**, *13*, 1149−1156.

(18) Liu, H.; Strobridge, F. C.; Borkiewicz, O. J.; Wiaderek, K. M.; Chapman, K. W.; Chupas, P. J.; Grey, C. P. Capturing metastable structures during high-rate cycling of $LiFePO_4$ nanoparticle electrodes. *Science (Washington, DC, U. S.)* **2014**, *344*, 1252817.

(19) Yamada, A.; Koizumi, H.; Nishimura, S.-I.; Sonoyama, N.; Kanno, R.; Yonemura, M.; Nakamura, T.; Kobayashi, Y. Room-temperature miscibility gap in Li_xFePO_4. *Nat. Mater.* **2006**, *5*, 357−360.

(20) Saravanan, K.; Jarry, A.; Kostecki, R.; Chen, G. A study of room-temperature $Li_xMn_{1.5}Ni_{0.5}O_4$ solid solutions. *Sci. Rep.* **2015**, *5*, 8027.

(21) Komatsu, H.; et al. Solid Solution Domains at Phase Transition Front of $Li_xNi_{0.5}Mn_{1.5}O_4$. *Adv. Energy Mater.* **2015**, *5*, 1500638.

(22) Huq, A.; Hodges, J. P.; Gourdon, O.; Heroux, L. Powgen: A third-generation high-resolution high-throughput powder diffraction instrument at the Spallation Neutron Source. *Zeitsch. Kristall. Proc.* **2011**, *1*, 127−135.

(23) Rodriguez-Carvajal, J. Recent advances in magnetic structure determination by neutron powder diffraction. *Phys. B (Amsterdam, Neth.)* **1993**, *192*, 55−69.

(24) Brown, I. D.; Altermatt, D. Bond-valence parameters obtained from a systematic analysis of the inorganic crystal structure database. *Acta Crystallogr., Sect. B: Struct. Sci.* **1985**, *41*, 244−247.

(25) Liu, Y.; Andrews, J. C.; Wang, J.; Meirer, F.; Zhu, P.; Wu, Z.; Pianetta, P. Phase retrieval using polychromatic illumination for transmission X-ray microscopy. *Opt. Express* **2011**, *19*, 540−545.

(26) Gryffroy, D.; Vandenberghe, R. E.; Legrand, E. A Neutron Diffraction Study of Some Spinel Compounds Containing Octahedral Ni and Mn at a 1:3 Ratio. *Mater. Sci. Forum* **1991**, *79-82*, 785−790.

(27) Shin, D. W.; Bridges, C. A.; Huq, A.; Paranthaman, M. P.; Manthiram, A. Role of Cation Ordering and Surface Segregation in High-Voltage Spinel $LiMn_{1.5}Ni_{0.5-x}M_xO_4$ (M = Cr, Fe, and Ga) Cathodes for Lithium-Ion Batteries. *Chem. Mater.* **2012**, *24*, 3720−3731.

(28) Kim, J.-H.; Huq, A.; Chi, M.; Pieczonka, N. P. W.; Lee, E.; Bridges, C. A.; Tessema, M. M.; Manthiram, A.; Persson, K. A.; Powell, B. R. Integrated Nano-Domains of Disordered and Ordered Spinel Phases in $LiNi_{0.5}Mn_{1.5}O_4$ for Li-Ion Batteries. *Chem. Mater.* **2014**, *26*, 4377−4386.

(29) Stöhr, J. *NEXAFS Spectroscopy*; Springer, 1992.

DOI: 10.1021/acs.chemmater.7b01898
Chem. Mater. 2017, 29, 6818−6828

(30) Yang, W.; Liu, X.; Qiao, R.; Olalde-Velasco, P.; Spear, J. D.; Roseguo, L.; Pepper, J. X.; Chuang, Y.-d.; Denlinger, J. D.; Hussain, Z. Key electronic states in lithium battery materials probed by soft X-ray spectroscopy. *J. Electron Spectrosc. Relat. Phenom.* **2013**, *190*, 64−74.
(31) Kan, W. H.; Chen, M.; Bae, J.-S.; Kim, B.-H.; Thangadurai, V. Determination of Fe oxidation states in the B-site ordered perovskite-type $Ba_2Ca_{0.67}Fe_{0.33}NbO_{6-\delta}$ at the surface (nano-scale) and bulk by variable temperature XPS and TGA and their impact on electrochemical catalysis. *J. Mater. Chem. A* **2014**, *2*, 8736−8741.
(32) Kan, W. H.; Dong, P.; Bae, J.-S.; Adams, S.; Thangadurai, V. Probing surface valence, magnetic property, and oxide ion diffusion pathway in B-site ordered perovskite-type $Ba_2Ca_{0.67}M_{0.33}NbO_{6-\delta}$ (M = Mn, Fe, Co). *Solid State Ionics* **2016**, *290*, 90−97.
(33) Sale, M.; Avdeev, M. 3DBVSMAPPER: a program for automatically generating bond-valence sum landscapes. *J. Appl. Crystallogr.* **2012**, *45*, 1054−1056.
(34) Nishimura, S.-i.; Kobayashi, G.; Ohoyama, K.; Kanno, R.; Yashima, M.; Yamada, A. Experimental visualization of lithium diffusion in Li_xFePO_4. *Nat. Mater.* **2008**, *7*, 707−711.
(35) Filso, M. O.; Turner, M. J.; Gibbs, G. V.; Adams, S.; Spackman, M. A.; Iversen, B. B. Visualizing Lithium-Ion Migration Pathways in Battery Materials. *Chem. - Eur. J.* **2013**, *19*, 15535−15544.
(36) Kishida, I.; Orita, K.; Nakamura, A.; Yokogawa, Y. Thermodynamic analysis using first-principles calculations of phases and structures of $Li_xNi_{0.5}Mn_{1.5}O_4$ ($0 \leq x \leq 1$). *J. Power Sources* **2013**, *241*, 1−5.

DOI: 10.1021/acs.chemmater.7b01898
Chem. Mater. 2017, 29, 6818−6828